The phototransduction machinery in the rod outer segment has a strong efficacy gradient

Monica Mazzolini[a,b,1], Giuseppe Facchetti[a,1], Laura Andolfi[b], Remo Proietti Zaccaria[c], Salvatore Tuccio[c], Johannes Treu[d], Claudio Altafini[a,2], Enzo M. Di Fabrizio[e,f], Marco Lazzarino[b,g], Gert Rapp[d], and Vincent Torre[a,3]

[a]International School for Advanced Studies, 34136 Trieste, Italy; [b]Cluster in Biomedicine S.c.r.l., 34149 Trieste, Italy; [c]Istituto Italiano di Tecnologia, 16163 Genova, Italy; [d]Rapp OptoElectronic, 22880 Wedel, Germany; [e]King Abdullah University of Science and Technology, Thuwal, 23955-6900, Saudi Arabia; [f]Bio-Nanotechnology and Engineering for Medicine, Department of Experimental and Clinical Medicine, University of Magna Graecia, 88100 Catanzaro, Italy; and [g]Istituto Officina dei Materiali - Consiglio Nazionale delle Ricerche, 34149 Trieste, Italy

Edited by King-Wai Yau, The Johns Hopkins University School of Medicine, Baltimore, MD, and approved April 13, 2015 (received for review December 4, 2014)

Rod photoreceptors consist of an outer segment (OS) and an inner segment. Inside the OS a biochemical machinery transforms the rhodopsin photoisomerization into electrical signal. This machinery has been treated as and is thought to be homogenous with marginal inhomogeneities. To verify this assumption, we developed a methodology based on special tapered optical fibers (TOFs) to deliver highly localized light stimulations. By using these TOFs, specific regions of the rod OS could be stimulated with spots of light highly confined in space. As the TOF is moved from the OS base toward its tip, the amplitude of saturating and single photon responses decreases, demonstrating that the efficacy of the transduction machinery is not uniform and is 5–10 times higher at the base than at the tip. This gradient of efficacy of the transduction machinery is attributed to a progressive depletion of the phosphodiesterase along the rod OS. Moreover we demonstrate that, using restricted spots of light, the duration of the photoresponse along the OS does not increase linearly with the light intensity as with diffuse light.

phototransduction | rhodopsin | phosphodiesterase | cGMP diffusion | optical fiber

Vertebrate photoreceptors, rods and cones, are morphologically specialized light sensing neurons and consist of four parts: an outer segment (OS), an inner segment (IS), the nuclear region, and the synapse (1). The OS of rod photoreceptors is stacked with thousands of lipid discs containing rhodopsin molecules that absorb photons (2–4). They are surrounded by a plasma membrane and differ in their lipid and protein composition.

It is known that within 1 s, each excited rhodopsin, densely packed in the disc membrane, activates tens of G proteins (named transducin), each of which activates one phosphodiesterase (PDE) molecule (5–7). Activated PDEs rapidly hydrolyze cytoplasmic cyclic guanosine monophosphate (cGMP) thereby closing cyclic nucleotide-gated (CNG) channels (8, 9). In darkness, a current carried by Na^+, K^+, and Ca^{2+} ions, which is known as the photocurrent, enters via the CNG channels into the OS and is pumped out by Na^+/K^+ ATPase, located in the IS (1). This current can be recorded using suction electrodes (3, 10).

The existence of distinct compartments on photoreceptor OSs is a consequence of their function. The OS is a highly modified nonmotile cilium developed for the absorption of light that is translated into the electrical signal. The IS and the nuclear region—containing the organelles and the nucleus—are dedicated to metabolism, homeostasis, and synthesis of the membrane and transportation of proteins and lipids supplied to the OS by an extensive trafficking through the tight restriction connecting the OS to the IS (11). Considering that, unlike typical cilia, the OS is continuously renewed throughout its entire life and given the varying density and asymmetry of the molecules involved, it is not surprising to find an efficacy gradient of phototransduction between the base and the tip. Indeed, the cholesterol (12, 13), the phospholipids (13–15), the CNG channels, the PDE (16), and the rhodopsin molecules (12) have different distributions between discs and plasma membranes; moreover, cholesterol (12, 13) and PDE (16) also have a different spatial distribution along the OS.

The biochemical machinery underlying phototransduction has been thoroughly investigated and described in a quantitative way (1). Previous studies in the early 1980s have demonstrated a lower sensitivity and slower kinetics of flash responses (3, 17, 18) at the tip of the OSs and that the amplitude of the single photon response is smaller at the OS tip than at the OS base (18). Despite these experimental observations, most of the models of phototransduction, developed subsequently, assumed a homogeneous efficacy of the transduction machinery along the OS (1, 19–22). In the present paper, by using highly confined spots of light obtained with apertureless tapered optical fibers (TOFs), we reveal that the biochemical machinery inside the rod OS has a gradient of efficacy much larger than previously thought (17, 18), demonstrating that the assumption of a homogeneous OS is not true. By using better technology, it is possible to obtain more confined spots of light necessary to uncover that OSs, not only have a specialized and different structure and function from that of ISs, but

Significance

Phototransduction is now considered to be a quite thoroughly understood phenomenon. It is well known that new discs are continuously generated at the base of the outer segments (OSs) and old discs are shed at their tip, but the rod OSs are considered a well-stirred compartment with minor inhomogeneities. To verify this assumption and to better understand the machinery within the OS, we developed a new methodology to deliver highly localized lights. We found that, as the light stimulus is moved from the OS base toward its tip, the amplitude of saturating and single photon responses decreased by 5–10 times. This gradient of efficacy is attributed to a progressive loss of phosphodiesterase. Therefore, OSs are highly inhomogeneous compartments.

Author contributions: M.M. and V.T. designed research; M.M., G.F., L.A., R.P.Z., S.T., J.T., C.A., E.M.D.F., M.L., and G.R. performed research; M.M., G.F., and V.T. analyzed data; M.M. performed experiments on rods; G.F. and C.A. performed modeling; L.A. and M.L. prepared and characterized the TOFs used in the experiments; R.P.Z., S.T., and E.M.D.F. performed fiber simulation; J.T. and G.R. designed the laser system; and M.M., G.F., and V.T. wrote the paper.

Conflict of interest statement: Some of the authors declare competing financial interests. V.T., M.M., M.L., and L.A. are listed as inventors in pending patent applications, and the International School for Advanced Studies and G.R. (Rapp OptoElectronic) are co-owners of the patent (European patent application no. 13195786.2-1652).

This article is a PNAS Direct Submission.

Freely available online through the PNAS open access option.

[1]M.M. and G.F. contributed equally to this work.

[2]Present address: Department of Electrical Engineering, Division of Automatic Control, Linkoping University, SE 58183, Linkoping, Sweden.

[3]To whom correspondence should be addressed. Email: torre@sissa.it.

This article contains supporting information online at www.pnas.org/lookup/suppl/doi:10.1073/pnas.1423162112/-/DCSupplemental.

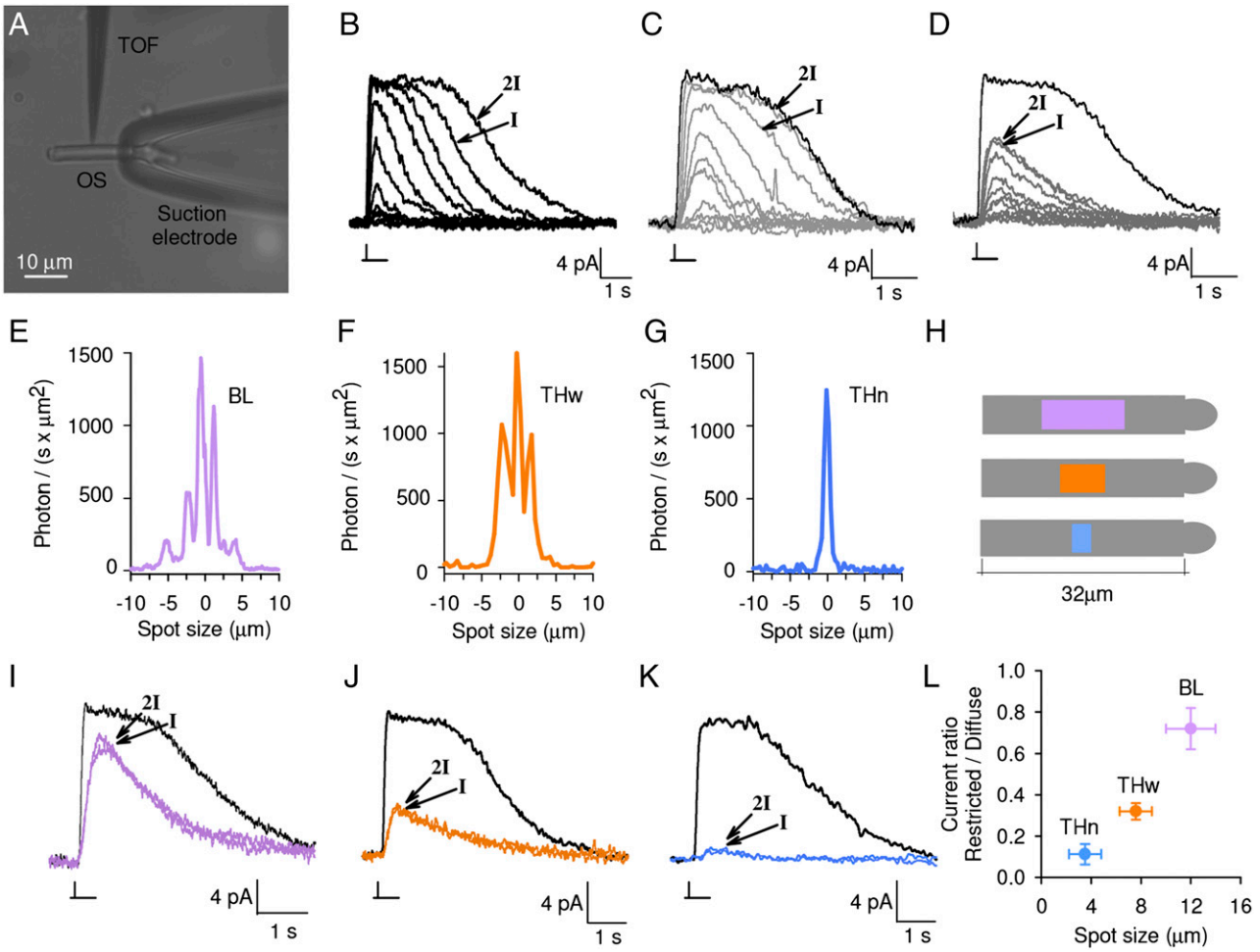

Fig. 1. Photoresponses and spot size from apertureless TOFs. (*A*) A rod in physical contact with the TOF. (*B*) Family of photoresponses to diffuse light of increasing intensity. (*C*) Family of light responses obtained from flashes of light delivered by the TOF with an aperture of 300 nm (gray traces) compared with the photoresponse obtained with a diffuse saturating light (black trace). Gray traces were obtained with light flashes which had a Gaussian profile. (*D*) Family of light responses obtained from flashes delivered by an apertureless TOF (dark gray traces) compared with the photoresponse obtained with a diffuse saturating light (black trace). (*E*–*G*) Lateral profiles of the light intensity (laser power 10 mW) at 5 µm fiber-sensor distance for three different apertureless TOFs (BL: Bessel-like, violet; THw: wide top-hat–like, orange; THn: narrow top-hat–like, blue). (*H*) The portion of the OS illuminated by the three TOFs (same color code). (*I*–*K*) Photoresponses (colored traces) obtained from saturating light flashes delivered to the OS middle by the apertureless TOFs with the profiles shown in *E*, *F*, and *G*, respectively, compared with the photoresponse obtained with a diffuse saturating light (black trace). The trace indicated by 2*I* was obtained from a light flash with intensity twice that indicated by *I* (the intensities *I* and 2*I* are saturating light). (*L*) Relation between spot size and fractional amplitude of the maximal photoresponse for the three different apertureless TOFs (more details in Fig. 2). Data were expressed as the mean ± SEM.

are also formed by inhomogeneous compartments (the internal discs) and that the efficiency of the transduction machinery is 5–10 times lower at the OS tip than at the base. A progressive depletion of PDE might represent a possible explanation of both this loss of efficacy and the role of PDE and cGMP diffusion in determining the peculiar kinetic features of the photoresponses we obtained by these highly confined flashes of light.

Results

The typical light exiting a conventional optical fiber resembles a Gaussian profile (23). To increase the spatial confinement of the exiting beam, therefore its resolution, we searched for optical fibers able to deliver highly localized light beams. In particular, we used commercially available apertureless TOFs with an Au/Ti metallic coating (*Materials and Methods*).

Photoresponses to Localized Spots of Light Produced by Apertureless Fibers. We compared the photoresponses of isolated rods from *Xenopus laevis* in response to conventional diffuse light and to restricted illumination (17, 18, 23) by using TOFs fed with a laser light of 491 nm. The IS of an isolated intact rod was drawn into a suction electrode (3, 10, 24, 25), which was then moved toward the TOF that was positioned orthogonally (Fig. 1*A* and *SI Appendix*, Fig. S1) touching the middle of the rod OS, so that its axis was at a distance less than 5 µm from the TOF apex. Photoresponses to diffuse light flashes had amplitude varying between 12 and 30 pA with the usual kinetics (Fig. 1*B*). If the TOF had a hole of 100–300 nm in its metallic coating, the exiting light exhibited a Gaussian profile. Light flashes produced by these TOFs evoked photoresponses that had a very similar amplitude and time course (gray traces in Fig. 1*C*) to those evoked by diffuse illuminations (black trace in Fig. 1*C*).

A different behavior was observed using apertureless TOFs (Fig. 1*D*): Photoresponses to saturating bright lights had smaller amplitudes with a different time course and did not increase in their duration when the light intensity was doubled (dark gray traces in Fig. 1*D*). Indeed, the amplitude and time course of the photoresponse to a saturating flash with the intensity 2*I* was very similar to the photoresponse to a flash of light with the intensity

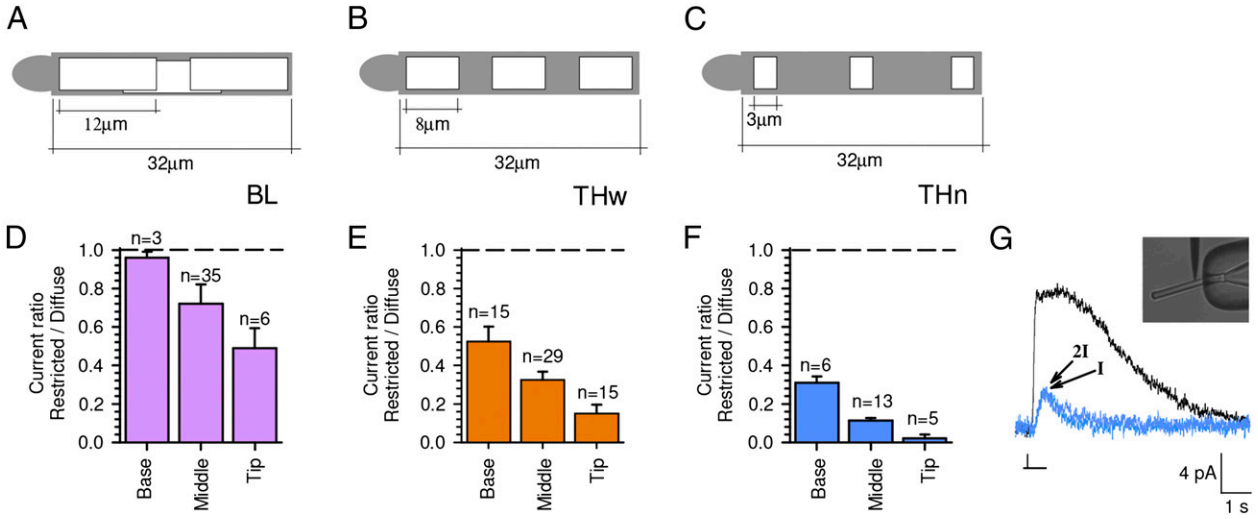

Fig. 2. Photoresponses from Bessel-like and top-hat–like TOFs. (*A–C*) Schematic representation of the illuminated portions of the OS by the three TOFs (Bessel-like, BL; wide top-hat–like, THw; and narrow top-hat–like, THn). (*D–F*) Average fractional amplitude of the maximal photoresponse at the base, middle, and tip using the three kinds of TOFs, illuminating the OS as in *A–C*. *E* corresponds to Fig. 4*D*. (*G*) Photoresponses (blue traces) obtained from flashes delivered to the OS base by the THn apertureless TOF compared with the photoresponse obtained with a diffuse saturating light (black trace). The trace indicated by 2*I* was obtained from a light flash with an intensity that was twice the intensity indicated by *I*. Mean ± SEM; *n*, number of experiments.

I, in sharp contrast with what was observed in the same rod but with diffuse light.

Therefore, we measured the wavefront of the exiting light of various TOFs and the corresponding evoked photoresponses, calculating the ratio of amplitude of saturating photoresponses to restricted and diffuse illuminations (Fig. 1 *E–L*). When the wavefront of the light exiting from apertureless TOFs had a Bessel-like (BL) profile with a width from 10 to 14 μm (Fig. 1*E*, BL) this ratio was equal to 0.72 ± 0.10. Wavefronts with a top-hat–like profile had a width of about 6–9 μm (top-hat–like wide, THw) (Fig. 1*F*, THw) and could also be narrower (top-hat–like narrow, THn) with a width from 2 to 5 μm (Fig. 1*G*, THn) and the corresponding ratios of evoked saturating photoresponses were equal to 0.32 ± 0.04 and 0.11 ± 0.05, respectively (Fig. 1 *J* and *K*, OS middle). With wavefronts reminiscent of a truncated Bessel function, the saturating photoresponses had an amplitude more similar to that of diffuse light (Fig. 1*I*) and were larger than those obtained with TOFs with a top-hat profile (Fig. 1*L*). A confirmation of these wavefront profiles was obtained with simulation analysis (*SI Appendix*, Figs. S3–S6). The THn was not extensively used because, at the OS tip, it did not elicit any detectable photoresponse (Fig. 2). Every time that we move the TOF along the OS, we also verify that the amplitude of the response obtained with the diffuse light is stable. With this procedure we rule out the possibility that the smaller photoresponses obtained with localized spots of light are caused by a progressive deterioration of responsiveness of isolated rods.

The BL, THw, and THn fibers produce on the OS spots of light with a diameter of ∼12, 8, and 3 μm, respectively (Fig. 2 *A–C*). When the BL TOF was used, the average fractional amplitude of the maximal photoresponse at the base, middle, and tip was 0.96 ± 0.03, 0.72 ± 0.10, 0.49 ± 0.10, respectively (Fig. 2*D*). These values decreased to 0.52 ± 0.08, 0.32 ± 0.04, and 0.15 ± 0.05 when the THw TOF was used (Fig. 2*E*) and no appreciable photoresponses could be detected at the tip of the OS when a THn TOF was used (Fig. 2*F*); in fact the average fractional amplitude of the maximal photoresponse at the base, middle, and tip was 0.31 ± 0.03, 0.11 ± 0.01, and 0.02 ± 0.02, respectively. When the base of OS was illuminated with a THn apertureless TOF, the average fractional amplitude of the maximal photoresponse was 0.31 ± 0.03 (compare black and blue traces in Fig. 2*G*) and when the light intensity was doubled, the time course of the photoresponse remained unaltered. Therefore, regardless of the type of profile, TOFs emitting a beam of light concentrated within 6–9 μm (Fig. 1 *F* and *L*, THw) were selected for our experiments described below.

We also used the rod itself as a light detector. In these experiments, when the TOF was at 1–3 μm from the OS center (Fig. 3*A*), a photoresponse of about 5 pA was recorded, which increased up to 12 pA when the OS center was at about 10 μm from the TOF apex (Fig. 3*B*), indicating that a large portion of the OS was illuminated. The photoresponse decreased to 8 pA when the OS was moved up by 30 μm (Fig. 3*C*), consistently with a decreased intensity of the light impinging on the OS. When the OS was moved laterally, the amplitude of the evoked photoresponse progressively decreased (Fig. 3*D*) and was about 1.5 pA when the TOF was moved to the OS tip (Fig. 3*E*). These observations indicate that the light exiting from the apertureless TOF has a significant far-field component highly confined in a cone exiting from its apex with an angle that varied from 10° to 30°. When the laser impinging on the apertureless TOF is switched on, the temperature of the TOF apex is expected to increase and this transient increase in temperature (26) could affect the photocurrent. This temperature increase diffuses in all directions and therefore we compared photoresponses when the OS was in the light cone exiting from the TOF (Fig. 3*E*) and at the same distance but with the OS outside the light cone (Fig. 3*F*). No photoresponses were evoked in these conditions, indicating that transient temperature increase has a negligible effect on rod photocurrent.

Phototransduction Has an Efficacy Gradient Along OS. We delivered restricted illuminations at various locations of the OS (Fig. 4, *Insets*) using light flashes with intensities increasing by three to four orders of magnitude, eliciting near threshold and saturating photoresponses. Photoresponses to diffuse (black traces) and restricted light (colored traces) differed in several fundamental features. First, when the base was illuminated (Fig. 4*A*), saturating photoresponses had fractional amplitudes equal to 0.52 ± 0.08 compared with those elicited by diffuse light (i.e., ∼50% of the dark current). When the middle was illuminated (Fig. 4*B*), the saturating photoresponses had lower fractional amplitudes of 0.32 ± 0.04 (Fig. 4*D*). At the tip of the OS (Fig. 4*C*), the

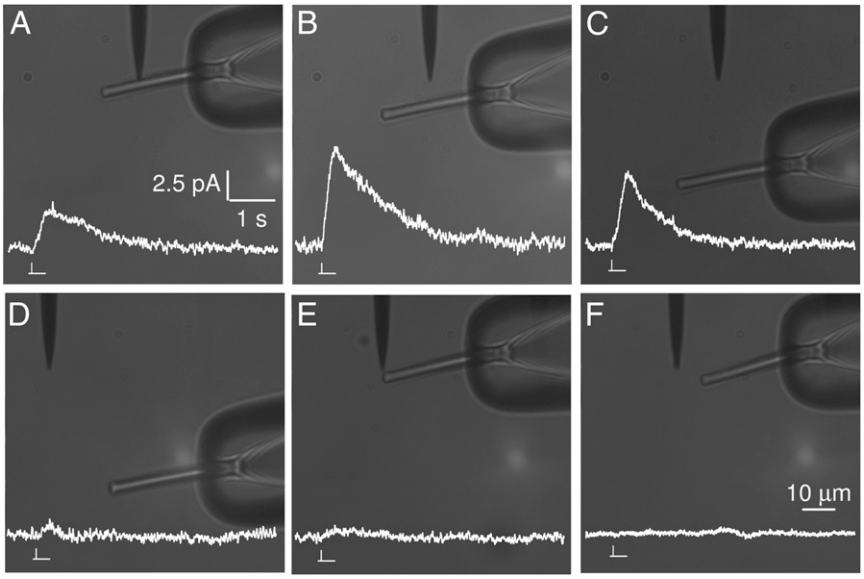

Fig. 3. Apertureless TOF characterization using a rod. (*A–F*) The apertureless TOF was moved in various positions showing different photoresponse amplitudes (saturating flash of light, 20-ms duration). The comparison of the current in *A* and *B* indicated that the light beam had a conical shape with an angle of about 30°. In addition, by increasing the distance, a larger portion of the OS was illuminated, and a larger photoresponse was recorded. By comparing traces in *C* and *D* (moving the TOF 20 μm), we inferred that this cone of light was restricted. Moving the TOF at the tip position of the OS, a significant decrease in the photoresponse was observed (*E*). When the fiber was slightly shifted to the rod OS (*F*), but within a close distance from it, no photoresponses were evoked.

photoresponses had fractional amplitudes of 0.15 ± 0.05 compared with the photoresponses evoked using diffuse light (Fig. 4*D*). Photoresponses to diffuse bright light peaked at 190 ± 4 ms (Fig. 4*E*), whereas photoresponses to restricted bright light peaked at 480 ± 40 ms, 560 ± 20 ms, and 620 ± 80 ms at the base, middle, and tip of the OS, respectively (Fig. 4*E*). The relation between light intensity I and the normalized amplitude of photoresponse A/A_{max} was fitted by the usual Michaelis–Menten relation (Fig. 4*F*) for diffuse illumination (black circles) and when apertureless TOFs (dark red, orange, and green circles) and TOFs with a hole of 100–300 nm (gray circles).

We computed also the spatial profile of the efficacy of the transduction machinery by displacing progressively the apertureless TOF from the rod OS base to its tip and vice versa. In the experiment shown in Fig. 5, the amplitudes of the saturating photoresponse at the base and middle of the OS were 13.4 pA and 6.6 pA, respectively (Fig. 5*A*). When the TOF was further moved toward the tip, the amplitude of the photoresponse decreased with an almost linear profile and was 2.5 pA near the tip and 1.5 pA at the very tip (Fig. 5 *A* and *B*). Collected data from more than 50 different experiments confirm that the efficacy of the phototransduction machinery decreases almost linearly from the base to near the tip (Fig. 5*C*).

Photoresponses caused by restricted illumination at various OS locations differed not only in amplitude (Fig. 4) but also in additional kinetic properties (Fig. 6), thus providing clues regarding the origin of the efficacy gradient of the phototransduction machinery. For this reason, we analyzed in details two parameters: the saturation time (T_S) and the slope of the rising phase (V). Using diffuse bright light of increasing intensity, the T_S (i.e., the period in which all CNG channels were closed) increased almost linearly with the logarithm of the light intensity (27) (Fig. 6*E*), but not with restricted illuminations. When photoresponses reached their maximal amplitude, they did not increase their duration when the light intensity was further increased (Fig. 6 *A–E*) (for details see *SI Appendix*, *SI Text*, section B). Moreover, whereas the time to peak of dim flash responses was longer at the tip than at the middle and at the base (*SI Appendix*, Fig. S8 *A* and *B*) the time course of the recovery following a not saturating photoresponse was similar (*SI Appendix*, Fig. S8*C*). The slope V of photoresponses increased with the diffuse brighter lights (Fig. 6*A*); in the presence of restricted lights (Fig. 6 *B–D*), V saturated at all locations and reached a plateau value (V_{max} proportional to the concentration of the total PDE; for details see *SI Appendix*, *SI Text* and Fig. S9), which was larger at the OS base than at its tip by nearly 10-fold (Fig. 6*F*). These observations suggest that a local saturation of the transduction machinery was reached during the rising phase of the photoresponses (Fig. 6*F*), i.e., before the intervention of the Ca^{2+} feedback (28) on the guanylate cyclase (GC) activity (29, 30), responsible for light adaptation, consistently with the linear relationship between V and the amplitude of photoresponse independent of the position of the light stimulus (Fig. 6*G*) and with the notion that the rising phase of photoresponses is not depending on the Ca^{2+} feedback (28).

We also confirmed that the conductance of CNG channels is similar along the OS, analyzing the current obtained with patch-clamp recordings (*SI Appendix*, Fig. S7). The strong gradient in the efficacy of the transduction machinery is likely associated with a lower amplification of the signaling cascade also present when very few photons are absorbed. Therefore, we investigated photoresponses to very dim flashes, as low as corresponding to a single photon absorption, and we compared photoresponses evoked by diffuse light and by TOF at the three positions. With diffuse light (Fig. 7*A*), we observed a significant variability with undetectable photoresponses (null events) as well as clear, single, and multiple events. From these data, we obtained amplitude histograms (Fig. 7*B*) revealing the expected quantal behavior described by the Poisson distribution with a single photon response of 0.29 ± 0.10 pA. Also at the OS base (Fig. 7*C*), we observed a significant variability with null, single, and multiple events. From these data, we obtained amplitude histograms (Fig. 7*D*) with a single photon response of 0.30 ± 0.11 pA. When the TOF was moved to the middle of the rod (Fig. 7*E*), similar single photon responses but with a smaller amplitude of 0.21 ± 0.12 pA (Fig. 7*F*) were observed, but not when the TOF was moved near the tip of the OS (Fig. 7 *G* and *H*). These results obtained in the same rod were confirmed in other

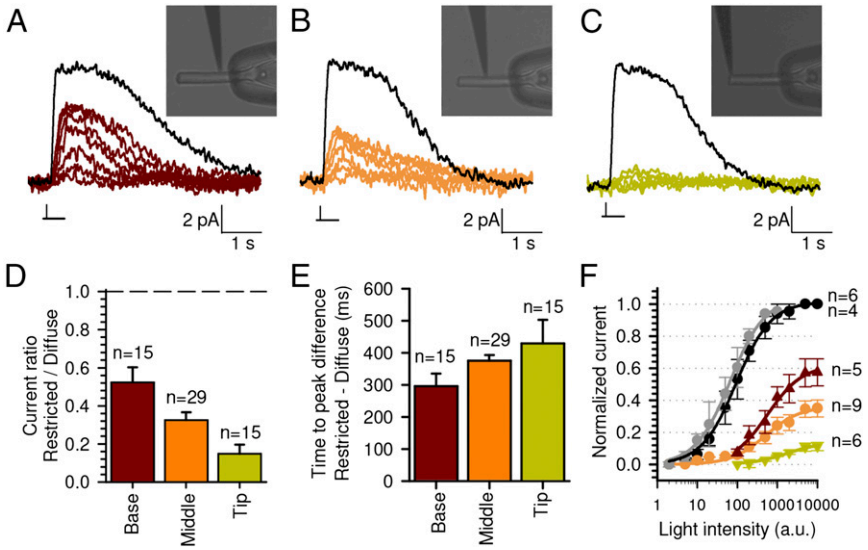

Fig. 4. The gradient of phototransduction efficacy along the OS. (*A*) Family of photoresponses obtained with the TOF touching the base of the OS (purple traces), compared with the photoresponse to a diffuse saturating flash of light (black trace). The color traces were obtained when the profile of the light reaching the rod OS was as in Fig. 1*F* and the laser power was 100, 200, 500, 1,000, 2,000, 5,000, and 10,000 μW, respectively. (*B*) As in *A* but with the TOF touching the middle (orange traces). (*C*) As in *A*, but with the TOF touching the tip (green traces). *Insets* in *A*–*C* represent the position of the TOF. (*D*) Average fractional amplitude of the maximal photoresponse. (*E*) Average difference of time to peak from saturating flashes. Photoresponses in *A*–*C* are from the same rod and the series of flashes delivered by the TOF have the same intensity. (*F*) Normalized current–intensity response with diffuse (black circles), with light from 100 to 300 nm TOF (gray circles) and restricted light for the base (dark red), middle (orange), and tip (green) positions. The solid lines were fitted according to $A = A_{max} \cdot I/(I + B)$ using the following parameters: A_{max} = 1.0, 1.0, 0.62, 0.36, and 0.14 and B = 87, 67, 570, 520, and 1,750 arbitrary units (a.u.) for responses with diffuse (black), 100–300 nm TOF (gray) and restricted (colored) light, respectively. Data were expressed as the mean ± SEM for *n* experiments.

rods. In three rods we compared the single photon response at the base and in the middle, and in five rods we could not see any single photon fluctuations at the OS tip but they were seen in the middle or at its base; as control, two rods were tested with diffuse light. In this case, the same illumination evoking clear photoresponses at the base and in the middle of the OS did not evoke any detectable photoresponse at the tip. When the flash intensity was further increased, small photoresponses were observed, which did not have the randomness expected from single photon events (Fig. 7 *I* and *J*), demonstrating that the reduction of efficacy is due to a reduced amplification and not to a lower probability of rhodopsin absorption. A confirmation is given by the same mean number of events per trial at the base and middle (Fig. 7). Moreover, because of its high density on the discs (25,000 Rh/μm^2), rhodopsin concentration cannot be responsible for the different kinetics and amplitude of the responses at each position and, especially, at each light intensity (also saturating). We can also rule out the possibility of a different photon absorbance along the OS, on the basis of the data shown in Fig. 7 *I* and *J*. Indeed if the difference between base and tip was due to a different number of Rh* (i.e., different absorbance), then by increasing the intensity of the flash, a single photon response would also appear at the tip, but this is not observed (Fig. 7 *I* and *J*). Thus, the null responses observed using diffuse flashes (3, 31) attributed to the failure in activating rhodopsin molecules could also be caused by the activation of a rhodopsin molecule at the tip of the OS, where the phototransduction is much less effective. We also noticed that the time course of the single photon response is very similar for restricted lights delivered at the base and at the middle of the rod OS (*SI Appendix*, Fig. S8*D*).

Discussion

The results here described show that, by using apertureless TOFs, it is possible to excite the rod OS with highly confined spots of light. In rod photoreceptors, when the TOF is moved from the OS base to its tip, the slope of the rising phase (Fig. 6*F*), the amplitude of saturating photoresponses (Fig. 4*D*), and the amplitude of the single photon response (Fig. 7) decrease about 5–10 times. Therefore, the phototransduction machinery at the tip is about 5–10 times less effective than at the base or at the middle of the OS.

Previous investigations also reported that the base of the rod OS was more sensitive than its tip (17, 18) by at most twofold. These differences were considered as minor deviations from a uniform distribution of the components of the biochemical machinery underlying phototransduction. Quantitative models (20–22), based on this assumption, were able to reproduce remarkably well almost all available experimental data, thus validating this assumption. However, the observation that the duration of the photoresponse, using restricted spots of light, does not increase linearly with the light intensity (Fig. 6 *B*–*E*) cannot be explained by any simple modification of these models (for details see *SI Appendix*, *SI Text*, section B, and Fig. S10). The differences about the saturation time between photoresponses obtained with restricted and diffuse light can be explained only by the existence of several compartments where the local concentration of key factors varies significantly and by the different diffusivity of these key factors between adjacent compartments (i.e., low or absent for rhodopsin, transducin, and PDE but significant for cGMP). In a homogeneous set of compartments the prolongation of the duration of photoresponses is caused by progressively stronger activation of the biochemical machinery. In the presence of many compartments the biochemical machinery will be differently activated by the light; in some of them the biochemical machinery will be saturated and photons absorbed will not contribute to the prolongation of photoresponses, which is caused only by photons absorbed in compartments where the biochemical machinery is not saturated. Therefore, appropriate models of phototransduction must be based on the use of a series of interconnected compartments (20–22). These models, however, will need a careful definition of many parameters inside the rod OS and it will be necessary to determine the concentration of the proteins known to be involved in phototransduction through

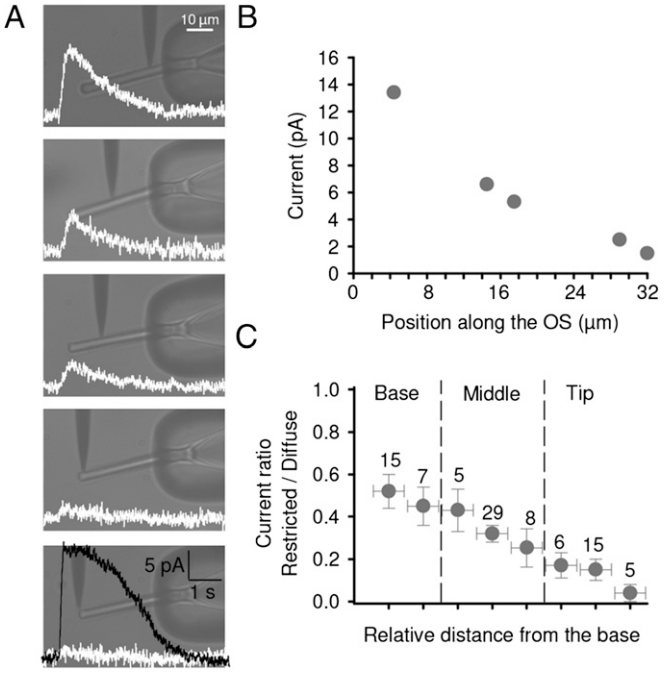

Fig. 5. Spatial profile of responsiveness along the OS. (*A*) The TOF was positioned at different locations along the OS of the same photoreceptor (same rod as in Fig. 3) and the photoresponses are recorded using a saturating light flash delivered by the TOF (white traces) compared with response obtained with saturating diffuse light (black trace). (*B*) Current amplitude of the saturating photoresponse, obtained with localized light, from the experiment shown in *A*. (*C*) The profile of the amplitude of the saturating photoresponse from different experiments (the number above each point indicates the number of averaged experiments). The three positions at the base, middle, and tip with n = 15, 29, and 15, respectively, are the same as in Fig. 4*D*. Distances from the rod OS base were normalized to the distance of the tip for individual OS.

cryosection methods (32), keeping in mind the existence of soluble and membrane-bound proteins.

The OS is continuously generated at their base during the entire life of the rod cells, probably as an initial invagination of the plasma membrane which then becomes sealed to generate mature discs (33); in this way, both old discs and plasma membranes (localized at the tip) are replaced simultaneously (33). The formation of new discs is balanced by the shedding at the OS tip (34), where old discs and plasma membrane are phagocytosed by the retinal pigment epithelium (RPE) (35) with a turnover ranging from about 10 days in mice (34) to 6–7 weeks in frogs (31, 34, 36). The molecular mechanisms for the degradation of distal photoreceptor OS and its role in phototransduction is still unknown (12, 16, 33, 36, 37). It is widely accepted that the ongoing renewal of discs is part of a normal process to replace and prevent the accumulation of damaged macromolecules. The principal source of damage is the continuous absorption of light that induces a photooxidative stress, which can be overcome by the renewal of the OS lacking of a common antioxidant defense system like glutathione (38). It is hypothesized that the mechanisms used by RPE to phagocytize are the same generally used for apoptotic cells. In fact a recent study (35) demonstrates that the phosphatidylserine (PS)—a normal lipid component of the OS membrane—becomes exposed, via specific scramblase, immediately before the disc shedding and the RPE thanks to a specific receptor–ligand interaction that is able to bind. However, the input that starts the tip shedding and the way that the aging of the discs causes the loss of efficacy have not been understood yet. Our study, revealing a gradient along the OS, suggests that the disc shedding is beneficial by removing the low efficacy tips of the OS.

It is known that the density of the CNG channels along the OS is uniform (33, 39, 40) and have the same conductance (*SI Appendix*, Fig. S7), therefore the observed gradient of efficacy is associated with the amplification steps between rhodopsin activation and the hydrolysis of cGMP molecules. Therefore, we asked which protein (i.e., rhodopsin, transducin, PDE) and which amplification step is responsible for the efficacy gradient. All these proteins are bound to the disc membrane: rhodopsin molecules span the membrane, whereas transducin and PDE (15) are peripherally anchored to the cytoplasmic surface of the discs. In particular, transducin is attached by weak hydrophobic and ionic interaction, whereas PDE by geranylgeranylation and farnesylation, and both are lipid composition dependent. In mouse, the diffusion coefficient for activated rhodopsin is 1.5 $\mu m^2/s$, for transducin, 2.2 $\mu m^2/s$, and for PDE, 1.2 $\mu m^2/s$. In salamander, the diffusion coefficient for activated rhodopsin is 0.7 $\mu m^2/s$, for transducin, 1.5 $\mu m^2/s$, and for PDE, 0.8 $\mu m^2/s$ (20, 22, 41). One rhodopsin molecule activates about 10 transducin molecules, one transducin molecule activates one PDE molecule, and one activated PDE hydrolyzes many cGMP molecules (1). Because the relative concentration of rhodopsin:transducin:PDE is 270:27:1 (1), in the case of restricted illumination, PDE—i.e., the less abundant protein—becomes the limiting factor of the amplification. Through a detailed analysis of the results and by a minimal mathematical model, we were able to exclude other limiting factors and any limiting kinetics (*SI Appendix*, *SI Text*, *section A* and Fig. S9). As a result, we propose that the limited availability of PDE is responsible for the saturation of the photoresponse elicited by restricted light. With diffuse light, in contrast, all discs are illuminated and the limiting factor is the number of available CNG channels: indeed on the entire rod OS the relative concentration of PDE:CNG channels is 25:1 (1). Therefore, the limited number of locally available PDE molecules could be responsible for the efficacy gradient along the OS. The longer delay in which photoresponses to restricted light reach their peak is presumably caused by the internal diffusion of the second messenger cGMP; activated PDEs in the illuminated compartment quickly hydrolyze cGMP molecules, whereas cGMP present in the neighboring compartments will diffuse inside. With diffuse light, this extra delay is not present because cGMP is hydrolyzed everywhere by the nearly uniform activation of PDEs. These results were used to estimate the cGMP diffusion coefficient (D_{cGMP}) (30, 37, 42). With our model (*SI Appendix*, *SI Text*, *section C* and Fig. S11), the value of the intracellular diffusion for cGMP is D_{cGMP} equal to 220 and 360 $\mu m^2/s$. Sensory transduction in vertebrate rods uses two intracellular messengers Ca^{2+} ions and cGMP molecules, which diffuse in very different ways: Ca^{2+} ions are highly buffered, act locally, and for this reason do not need a fast diffusion (30), whereas cGMP molecules diffuse easily and counterbalance the inhomogeneity of phototransduction efficacy inside the OS. If the phototransduction machinery demonstrates a high gradient of efficacy, then how can light close CNG channels at the tip of the rod OS, where the phototransduction machinery is not so efficient? The relatively high value of D_{cGMP} provides insight to this question: CNG channels at the tip of the OS are closed because cGMP molecules diffuse toward the PDE molecules activated by light.

Compartmentalization as a basic feature of the transduction machinery in rods could also be a characteristic of other sensory neurons, such as cones (38, 43) and olfactory sensory neurons (44–47) and could explain the high turnover and renewal of these cells. Not only sensory neurons, which have an intrinsic functional specialization, are likely to be compartmentalized but possibly the great majority of cells have a similar internal organization. Indeed, the existence of micro and nano domains of Ca^{2+} ions inside cells is well known (48) and compartmentalization

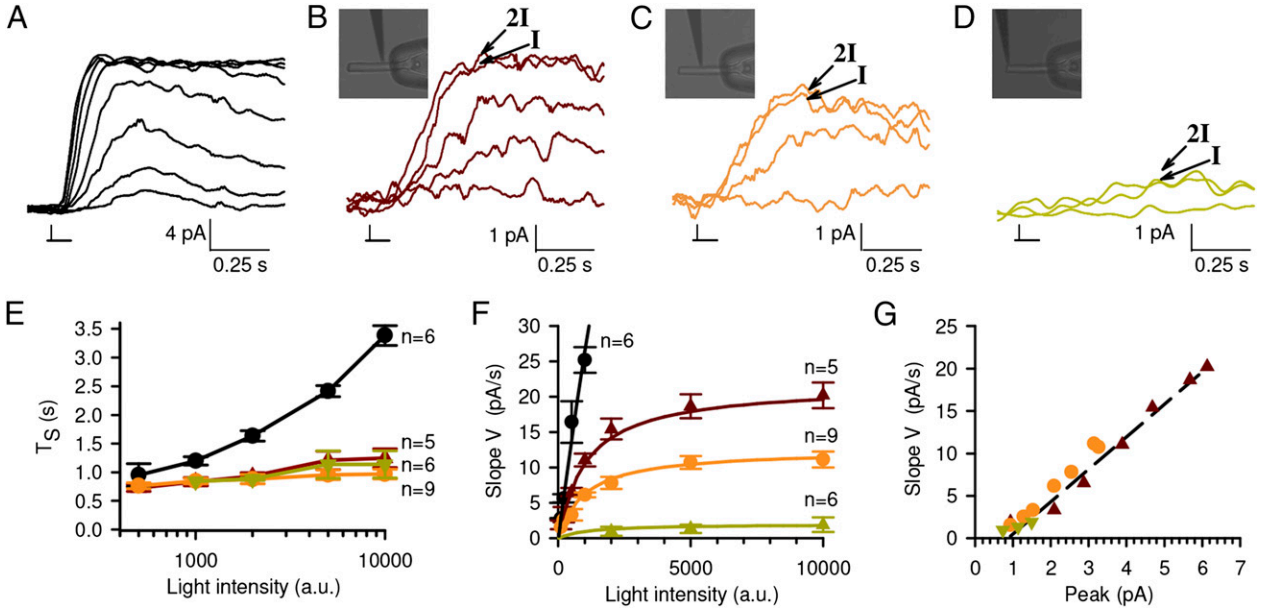

Fig. 6. Different phototransduction kinetics along the OS. (*A*) Expanded scale for a family of selected photoresponses (Fig. 1*B*) to diffuse light of increasing intensity. (*B*) The same as in *A* but touching the base (purple traces) of the OS with TOF (Fig. 4*A*). (*C*) As in *A* but with the TOF touching the middle (orange traces) (Fig. 4*B*). (*D*) As in *A*, but with the TOF touching the tip (green traces) (Fig. 4*C*). (*E*) Relationship between the light intensity and the T_s, measured from the flash until 20% recovery of the current. (*F*) Relationship between light intensity and the slope of the rising phase of photoresponses; fit with the equation $V = V_{max} \cdot I/(I + K_s)$ with the following parameters: V_{max} = 27.7, 12.6, 2.5 pA/s (base, middle, and tip, respectively) and K_s = 1,100 a.u. (for details about our model and about the meaning of these parameters see *SI Appendix, SI Text* and Fig. S9). (*G*) Linear relationship between the peak amplitude of evoked photoresponse and *V*. The light intensity in *E* and *F*, which is in arbitrary units (a.u.), is different between diffuse and restricted illuminations. Mean ± SEM; *n*, number of rods.

of the cell interior seems a requirement for the appropriate functioning of second messengers, such as Ca^{2+} ions and cyclic nucleotides. The existence of membrane-bound and cytosolic forms of proteins with different diffusion coefficients (49) is another ingredient of the widespread compartmentalization inside cells.

Recent developments of chemistry have provided biology with an increasing number of light-sensitive compounds with major biological relevance. There is now a large selection of caged molecules that can be released by light photolysis (50), such as calcium ions (51), glutamate (52), and GABA (53) The engineering of light-sensitive ion channels, such as the light-activated glutamate channel (54), the light-activated potassium channels (55), and those based on modifications of the rhodopsin molecule, such as the light-gated proton channel, channelrhodopsin (56), and the choloride ion pump halorhodopsin (57), offer biologists powerful tools to investigate both the cellular compartmentalization and the organization of neuronal networks. A light switch can also be inserted in metabotropic receptors such as the adrenergic receptor (58) and in specific proteins such as Rac (59). These novel probes also provide the opportunity to analyze the biological effects of the activation of a reduced number of ion channels, receptors, and proteins possibly at a single molecule level (60). In this case, it is mandatory to have light beams with well-defined wavefront profiles, possibly without the Gaussian lobes present when standard light sources are used. With conventional optical components it is certainly possible to have spots smaller than 1 μm, but only by using high numerical aperture (N.A.) objectives (larger than 1–1.3), which are not ideal for electrophysiological experiments when it is necessary to have a visual control during the manipulation of electrodes and cells. Apertureless TOFs produce spots of light confined in a cylinder of height of about 10 μm with a diameter that could be varied from 2 to 14 μm (Fig. 1*H*). By exciting the rod OS with these TOFs, novel properties of phototransduction are obtained. These apertureless TOFs can also be used in optogenetics, for the activation of light-sensitive ion channels in specific regions of a neuron such as distal dendrites and/or single spines of a cell. These TOFs allow the activation of a very limited number of light-sensitive receptors and proteins and to investigate their efficacy with unprecedented accuracy. Highly confined spots of light could be obtained with TOFs with microoptics at their tip (61) producing top-hat–like wavefronts propagating over some tens of micrometers with specific width and with a limited divergence.

Materials and Methods

Isolated Photoreceptors from the Retina. Dissociated rods were obtained from adult male *Xenopus laevis* frogs (*Xenopus* express, Ancienne Ecole de Vernassal, Le Bourg, France) as previously reported (62, 63). OS lengths for green-sensitive and blue-sensitive rods (64) where 31 ± 1 μm (n = 85) and 26 ± 1.5 μm (n = 17), respectively, and the OS diameter is about 4–6 μm. All experiments performed in this study were approved by the International School for Advanced Studies Ethics Committee according to the Italian and European guidelines for animal care (d.l. 116/92; 86/609/C.E.). The frogs were dark-adapted overnight, and their eyes were enucleated and hemisected under a dissecting microscope with infrared illumination (wavelength: 820 nm). Isolated and intact rods were obtained by mechanical dissociation and immersed in Ringer's solution containing the following (in millimoles): 110 NaCl, 2.5 KCl, 1 $CaCl_2$, 1.6 $MgCl_2$, and 3 Hepes-NaOH, 0.01 EDTA, and 10 glucose (pH 7.7–7.8 buffered with NaOH). All chemicals were purchased from Sigma-Aldrich. After dissociation, the sample was transferred into a silanized recording chamber. All experiments were performed at room temperature (22–24 °C). All images were acquired using ProgRes Capture Pro v2.8.0 under infrared light (wavelength: 900 nm) using Jenoptic ProgRes MF camera.

Photoresponse Recordings. After mechanical isolation (Fig. 1*A* and *SI Appendix*, Fig. S1), the IS of an isolated and intact rod was drawn (25) into a silane-coated (17) borosilicate glass electrode (Blaubrand, intramark micropipette) (internal diameter of 4–6 μm) filled with Ringer's solution. Rods were viewed under infrared light (wavelength: 900 nm) using two cameras (Olympus XM10 and Jenoptic ProgRes MF) at two magnifications and stimulated with 491 nm diffuse light (Rapp OptoElectronic), which emerged

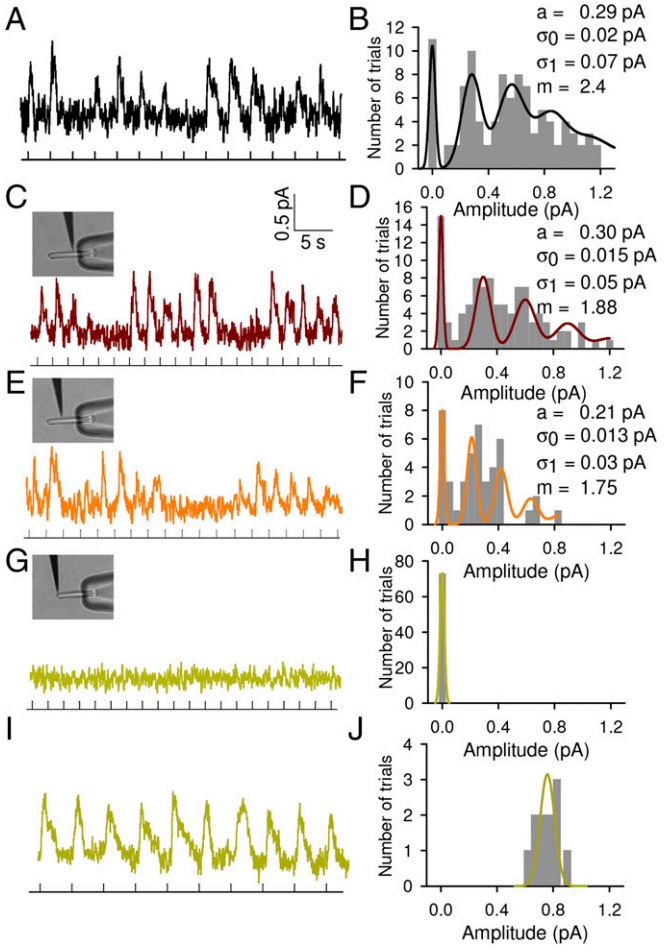

Fig. 7. Single photon responses. (*A*) Photoresponses evoked by diffuse dim flashes of light. (*B*) Histogram of the amplitudes of evoked photoresponses fitted as described (n = 100). (*C*) Photoresponses evoked by dim flashes of light delivered at the indicated times by the TOF touching the base of the OS. (*D*) Histogram of the amplitudes of evoked photoresponses fitted as described (n = 100). (*E* and *F*) As in *C* and *D*, but when the TOF touched the middle (n = 44). (*G* and *H*) As in *C* and *D*, but when the TOF touched the tip (n = 70). (*I* and *J*) As in *G* and *H*, but increasing the flash intensity by 50 times (n = 9). *Insets* in *C*, *E*, and *G* represent the position of the TOF. The histograms (bin = 0.05 pA) were fitted with the equation described in *Materials and Methods*: values providing the best fit were reported; a is the mean response to single photon, σ_0 is the noise SD, σ_1 is the SD of the mean, and m is the mean number of events per trial. For diffuse, base, and middle the ensemble variance (σ^2) is 0.08, 0.12, and 0.05 pA^2, respectively, and the ratio between σ^2 and mean of responses is 0.24, 0.31, and 0.18 pA, respectively.

from the 10× objective of an inverted microscope (Olympus IX71). If the maximal photoresponse was more than 12 pA, then the rod was selected for the experiment. The restricted light was applied using an apertureless TOF coated with gold/titanium (LovaLite, Besançon), and the OS was moved against the tip of the TOF to obtain physical contact, ensuring that the rod and fiber were in the same optical plane. To rule out the possible light scattering during the stimulation at the base of the rod OS, we normally have the TOF tip at a distance from the suction pipette of 3–4 μm. If photoresponses to diffuse lights were identical before and after physical contact, photoresponses to restricted lights were investigated. The recorded photoresponses was similar for green-sensitive (named also principal "red") and for blue-sensitive ("green") rods (64). The TOF was mounted on a micromanipulator (EXFO motorized manipulator PCS-6000) to allow the movement of the tip along the three axes. Photoresponses to brief light flashes (duration 20 ms at various laser intensities) were recorded as previously described (3, 10, 24, 25) using an Axopatch 200A (Molecular Devices) in voltage clamp mode. The duration of used flashes is shorter than the lifetime of activated rhodopsin (about 40–50 ms) (65). Fig. 1*F* shows that with our TOF, we deliver about 1,000 photon/(s × μm^2), which implies about 20 photon/μm^2. With diffuse light the increasing laser intensities correspond to 1, 3, 6, 15, 30, 60, 120, 315, 630, 125, 3,100, and 6,300 photoisomerizations (Rh*). Photoresponses in Fig. 4 *A*–*C* are from the same rod and the series of flashes delivered by the TOF have the same intensity from dim to bright light corresponding to 3, 5, 15, 25, 50, 130, and 260 Rh* for base position; 3, 6, 15, 28, 55, 135, and 280 Rh* for middle; and 2, 5, 12, 25, 50, 115, and 230 Rh* for tip. For the colored traces obtained with apertureless TOFs, the laser power was 5, 10, 20, 50, 100, 200, 500, 1,000, 2,000, 5,000, and 10,000 μW, respectively. The family of light responses obtained from flashes of light delivered by the TOF with an aperture of 1 μm, the laser power was equal to 1, 2, 5, 10, 20, 50, 100, 200, 500, and 1,000 μW, respectively. See figure legends in the main text for details. The current was low-pass filtered at 20 Hz and digitized at 100 Hz. In all of the experiments, a saturating response was periodically measured to confirm the stability of the rod.

Cameras and Laser System. Experiments often require visualization of the sample at different magnification levels. However, changing objectives causes mechanical vibration that in turn may lead to loss of the patch (or stability between rod, suction electrode, and TOF). We therefore developed a dual camera port with different magnification. The layout and the performance of this system is shown in *SI Appendix*, Fig. S1. The basic requirements for the system to stimulate the OS of the photoreceptors were (*i*) stable and reproducible laser power and (*ii*) the possibility to program pulse trains of arbitrary length with intensities over a broad dynamic range of four to five orders of magnitude. We set up a system consisting of a highly stable continuous 491-nm laser module, an acoustooptic modulator (AOM), a rapid filter wheel with a set of neutral density filters to attenuate the beam, three ports for fiber optics with shutters on each port, a microcontroller, and software to program pulse trains. The AOM served as a rapid switch for the laser and additionally for attenuating the beam over almost two orders of magnitude. The filter wheel was equipped with neutral density filters of OD1, OD2, and OD3. Hence, the dynamic range of the system covered almost five orders of magnitude. Two TOFs and one light guide for diffuse illumination were connected to the fiberoptic ports.

Localized Excitation of OS Using Apertureless TOF Versus Generation of Small Spots via Conventional Microscope Optics. To perform electrophysiological experiments as those described in the main text and in the great majority of electrophysiological and optogenetic investigations, it is very useful and possibly mandatory to have a wide field of view and a large depth of field. Both requirements are met using low magnification objectives. Such objectives usually have a low N.A.. With conventional optical components, it is certainly possible to generate spots on the order of millimeters or even smaller. In the ideal case of an aberration-free optical system, the diameter (D) of the focal spot depends on the N.A. of the objective and on the illumination wavelength (λ) and is given by $D = 1.22 \cdot \lambda / \text{N.A.}$

For a typical 10× objective with N.A. 0.25 and a wavelength of 500 nm, in the ideal case the spot size is about 2.44 μm, but in practice it will be significantly larger. In the ideal case, spots on the order of 1 μm can be obtained with objectives with N.A. >0.6. However, such objectives have high magnification with small field of view and small depth of field. Considering the second requirement of large depth of field, again a low N.A. objective is required. As derived by Berek in 1927 (66), the depth of field (DOF, in micrometers) in a microscope can be calculated as $\pm\text{DOF} = [350/(\text{N.A.} + M)] + (\lambda/(2 \cdot \text{N.A.}^2))$, with M = total magnification = objective magnification*eyepiece magnification (typically 10×). Berek's equation (66) can also be used in camera-based systems as an approximation. However, here the DOF depends on the number of pixels of the camera, the optical magnification of the camera adaptor, and the numerical aperture. As an approximation, for λ = 500 nm, eye-piece magnification for a 10× objective, N.A. 0.25, M = 100, we have ±DOF = 18 μm; and for a 100× objective, N.A. 1.0, M = 1,000, we have ±DOF = 0.6 μm. A further drawback when generating a small spot using the microscope optics is the scattered light from the cone of light along the optical path. In particular with highly light sensitive objects like rod OS, scattered light will distort the measurements. These considerations show that, to have small spots of light in a confined 3D region, the use of apertureless TOFs is highly valuable, if not mandatory.

Single Photon Response Analysis. Single photon responses were evoked by a series of 50–100 dim flashes of light delivered every 4 s, with duration of 20 ms each, by diffuse light and by the TOF touching the three positions (base, middle, and tip) of the OS. Responses to a single photoisomerization were interspersed from failures or multiple photoisomerizations. The mean response was fitted using the equation from Rieke and Baylor (25) and the

obtained histograms (bin = 0.05 pA) were fitted with the equation from Baylor (3).

Optical Characterization of Tapered Optical Fiber. The gold on the titanium layer coated apertureless single mode TOF (Au coating 100 nm thickness, N.A. 0.1, internal core diameter, 8 μm) (LovaLite, Besançon) used to stimulate a confined part of a single rod cell was optically characterized by measuring the profile of emitted light in a perpendicular plane as a function of displacement in z direction from its tip by using a scanning near-field optical microscopy system (SNOM) (APE Research). The SNOM head was placed on an inverted optical microscope (Zeiss Axiovert 200), suitable for working in transmission mode. The TOF was attached to a tuning fork that oscillated at its resonance frequency (32 kHz), when the fiber was in the proximity of the sample; shear-forces interactions damped this motion and induced measurable changes in the oscillation amplitude. An electronic feedback system was subsequently used to maintain constant this oscillation amplitude. The fiber-sample distance was modulated by using a piezo-driven z movement that allows moving the sample stage for the characterization of the light exiting from the fiber as a function of distance. For optical measurements, a laser light (wavelength: 491 nm) was coupled to a single-mode optical fiber (Thorlabs) welded to the apertureless TOF. The light emerging from the fiber apex was collected by a 40× objective lens (0.6 N.A.) or a 100× objective lens (0.8 N.A.) located below the sample and detected by a CCD camera (DVC-1412 AM monochrome digital camera QE > 62% at 550 nm). We measured the radius of the spot using the CCD camera and the center of the spot was identified as the brightest pixel. Six to eight line segments were drawn through the center of the spot and for each of these segments we computed the intensity profile. Next, we determined the distance from the center of the spot for which the intensity was at least twice the dark noise measured by the CCD camera. The mean distance obtained from the six to eight segments was taken as the spot radius. We found that light exits also from commercially available apertureless tapered optical fibers, such as shown in *SI Appendix*, Fig. S2*O*. When a laser light (491 nm) was fed into these apertureless TOFs the front wave of the exiting light had two main behaviors. In some cases, at distances z between 1 and 10 μm from the TOF apex the wavefront had almost symmetrical rings (*SI Appendix*, Fig. S2) with a light profile reminiscent of a truncated Bessel profile and in other cases the light wavefront was more concentrated around its center with an almost top-hat profile. At distances larger than 20 μm the wavefront diverged and often a brighter ring of light appeared at the border of the profile, as opposed to what is observed in Bessel and Gaussian beams. The width of the front wave of top-hat–like profiles remained confined between 2 and 9 μm for distances up to 10 μm and the light intensity at the center of the wavefront decreased with the distance z as $1/z$. These observations suggest that the tapered shape of these optical fibers act as optical components with properties reminiscent of conical lenses, called axicons (67) that transform a Gaussian into a Bessel beam (68, 69). In some cases at the end of the experiment, we fully characterized the light exiting from the used TOF so to relate properties of the evoked photoresponse to the profile of the light impinging on the rod. Here, the light profile was measured at different distances from the OS and the size and intensity of the spot of light as a function of the distance was measured. The number of photons emitted from the TOF apex increased linearly with the laser power. Focused ion beam (FIB) was used to generate an aperture of about 100–300 nm in its metallic coating at the apex of the TOF used for the experiments in Figs. 1*C* and 4*F*.

Simulation of Apertureless Tapered Optical Fiber. To understand the origin of the measured light profiles (Fig. 1) we have investigated, through full 3D numerical simulations, the light profile—or more precisely the electrical field—emerging from apertureless TOFs with different geometries (*SI Appendix*, Figs. S3–S6). We have modeled a TOF as a 3D dielectric cone covered by gold (Au). The overall simulated domain was 15 μm × 15 μm × 15 μm for a resolution down to 10 nm at the Au coating layer. We have analyzed in detail the role of the apex shape and of its angle. There are three main simulated structures: ideal conical apex, rounded conical apex, and cut-edge conical apex. All of the configurations have SiO_2 core material coated with 100 nm of Au. The base of the cone has a radius $R = 1$ μm. The rounded conical structure shows a SiO_2 radius of curvature of 200 nm. Similarly, the cut-edge cone, has a SiO_2 disc radius $r = 200$ nm. The incoming light is a Gaussian beam polarized along x direction and impinging along the z direction. We have chosen three different wavelengths, 442 nm, 491 nm (corresponding to the experimental excitation), and 633 nm, to verify the robustness of the fibers under wavelength change. Our numerical simulations indicate some basic relations between the geometrical features of apertureless TOFs and the emitted light profile: (*i*) for small apex angle, the emitted light profile is dominated by diffraction; (*ii*) for large apex angle, the emitted light has an axicon-like behavior; and (*iii*) the apex shape is important for small apex angles, whereas it is "negligible" for large apex angles. These characteristics can be understood by observing the E_x and E_z amplitude distributions (electric field on the xz plane at about 5 μm from the tip end) at small and large apex angles. It is found that the zero field region associated with the E_z component, which is distributed along the cone axis, tends to "collapse" for big apex angles; therefore, field distributions with a large central lobe are expected. The opposite behavior is seen for small apex angles, where the cone tends to reflect the optical behavior of a cylinder undergoing a transversal optical excitation, which provides a zero field region along its axis.

ACKNOWLEDGMENTS. We thank Profs. Trevor Lamb and Fabio Benfenati for reading the manuscript, M. Lough for checking the English, and Paolo Fabris for MatLab support. This work was supported by FOCUS Contract 270483 (FP7-ICT-2009-6) from the European Union.

1. Pugh EN, Jr, Lamb TD (2000) *Phototransduction in Vertebrate Rods and Cones: Molecular Mechanisms of Amplification, Recovery and Light Adaptation. Handbook of Biological Physics* (Elsevier, Amsterdam), pp 183–255.
2. Yoshizawa T, Wald G (1963) Pre-lumirhodopsin and the bleaching of visual pigments. *Nature* 197:1279–1286.
3. Baylor DA, Lamb TD, Yau KW (1979) Responses of retinal rods to single photons. *J Physiol* 288:613–634.
4. Kwok-Keung Fung B, Stryer L (1980) Photolyzed rhodopsin catalyzes the exchange of GTP for bound GDP in retinal rod outer segments. *Proc Natl Acad Sci USA* 77(5): 2500–2504.
5. Baehr W, Devlin MJ, Applebury ML (1979) Isolation and characterization of cGMP phosphodiesterase from bovine rod outer segments. *J Biol Chem* 254(22):11669–11677.
6. Dumke CL, Arshavsky VY, Calvert PD, Bownds MD, Pugh EN, Jr (1994) Rod outer segment structure influences the apparent kinetic parameters of cyclic GMP phosphodiesterase. *J Gen Physiol* 103(6):1071–1098.
7. Leskov IB, et al. (2000) The gain of rod phototransduction: Reconciliation of biochemical and electrophysiological measurements. *Neuron* 27(3):525–537.
8. Fesenko EE, Kolesnikov SS, Lyubarsky AL (1985) Induction by cyclic GMP of cationic conductance in plasma membrane of retinal rod outer segment. *Nature* 313(6000): 310–313.
9. Kaupp UB, Seifert R (2002) Cyclic nucleotide-gated ion channels. *Physiol Rev* 82(3):769–824.
10. Baylor DA, Lamb TD, Yau KW (1979) The membrane current of single rod outer segments. *J Physiol* 288:589–611.
11. Pearring JN, Salinas RY, Baker SA, Arshavsky VY (2013) Protein sorting, targeting and trafficking in photoreceptor cells. *Prog Retin Eye Res* 36:24–51.
12. Boesze-Battaglia K, Fliesler SJ, Albert AD (1990) Relationship of cholesterol content to spatial distribution and age of disc membranes in retinal rod outer segments. *J Biol Chem* 265(31):18867–18870.
13. Albert AD, Young JE, Paw Z (1998) Phospholipid fatty acyl spatial distribution in bovine rod outer segment disk membranes. *Biochim Biophys Acta* 1368(1):52–60.
14. Melia TJ, Malinski JA, He F, Wensel TG (2000) Enhancement of phototransduction protein interactions by lipid surfaces. *J Biol Chem* 275(5):3535–3542.
15. Hessel E, Heck M, Müller P, Herrmann A, Hofmann KP (2003) Signal transduction in the visual cascade involves specific lipid-protein interactions. *J Biol Chem* 278(25): 22853–22860.
16. Nishizawa Y, Yamazaki A, Usukura J (2004) Electron microscopic localization of PDE α, β and δ in frog retina. *Invest Ophthalmol Vis Sci* 45(5):5353.
17. Lamb TD, McNaughton PA, Yau KW (1981) Spatial spread of activation and background desensitization in toad rod outer segments. *J Physiol* 319:463–496.
18. Schnapf JL (1983) Dependence of the single photon response on longitudinal position of absorption in toad rod outer segments. *J Physiol* 343:147–159.
19. Lamb TD, Pugh EN, Jr (1992) A quantitative account of the activation steps involved in phototransduction in amphibian photoreceptors. *J Physiol* 449:719–758.
20. Bisegna P, et al. (2008) Diffusion of the second messengers in the cytoplasm acts as a variability suppressor of the single photon response in vertebrate phototransduction. *Biophys J* 94(9):3363–3383.
21. Shen L, et al. (2010) Dynamics of mouse rod phototransduction and its sensitivity to variation of key parameters. *IET Syst Biol* 4(1):12–32.
22. Caruso G, et al. (2011) Identification of key factors that reduce the variability of the single photon response. *Proc Natl Acad Sci USA* 108(19):7804–7807.
23. Sim N, Bessarab D, Jones CM, Krivitsky L (2011) Method of targeted delivery of laser beam to isolated retinal rods by fiber optics. *Biomed Opt Express* 2(11):2926–2933.
24. Forti S, Menini A, Rispoli G, Torre V (1989) Kinetics of phototransduction in retinal rods of the newt Triturus cristatus. *J Physiol* 419:265–295.
25. Rieke F, Baylor DA (1998) Origin of reproducibility in the responses of retinal rods to single photons. *Biophys J* 75(4):1836–1857.
26. Lamb TD (1984) Effects of temperature changes on toad rod photocurrents. *J Physiol* 346:557–578.
27. Calvert PD, et al. (2001) Membrane protein diffusion sets the speed of rod phototransduction. *Nature* 411(6833):90–94.

28. Torre V, Matthews HR, Lamb TD (1986) Role of calcium in regulating the cyclic GMP cascade of phototransduction in retinal rods. *Proc Natl Acad Sci USA* 83(18):7109–7113.
29. Krizaj D, Copenhagen DR (2002) Calcium regulation in photoreceptors. *Front Biosci* 7: d2023–d2044.
30. Nakatani K, Chen C, Koutalos Y (2002) Calcium diffusion coefficient in rod photoreceptor outer segments. *Biophys J* 82(2):728–739.
31. Solessio E, et al. (2004) Developmental regulation of calcium-dependent feedback in Xenopus rods. *J Gen Physiol* 124(5):569–585.
32. Sokolov M, et al. (2002) Massive light-driven translocation of transducin between the two major compartments of rod cells: A novel mechanism of light adaptation. *Neuron* 28(1):34:95–106.
33. Nemet I, Tian G, Imanishi Y (2014) Submembrane assembly and renewal of rod photoreceptor cGMP-gated channel: Insight into the actin-dependent process of outer segment morphogenesis. *J Neurosci* 34(24):8164–8174.
34. Young RW (1967) The renewal of photoreceptor cell outer segments. *J Cell Biol* 33(1): 61–72.
35. Ruggiero L, Connor MP, Chen J, Langen R, Finnemann SC (2012) Diurnal, localized exposure of phosphatidylserine by rod outer segment tips in wild-type but not Itgb5-/- or Mfge8-/- mouse retina. *Proc Natl Acad Sci USA* 109(21):8145–8148.
36. Sung CH, Chuang JZ (2010) The cell biology of vision. *J Cell Biol* 190(6):953–963.
37. Gross OP, Pugh EN, Jr, Burns ME (2012) Calcium feedback to cGMP synthesis strongly attenuates single-photon responses driven by long rhodopsin lifetimes. *Neuron* 76(2): 370–382.
38. Winkler BS (2008) An hypothesis to account for the renewal of outer segments in rod and cone photoreceptor cells: Renewal as a surrogate antioxidant. *Invest Ophthalmol Vis Sci* 49(8):3259–3261.
39. Watanabe S, Matthews G (1988) Regional distribution of cGMP-activated ion channels in the plasma membrane of the rod photoreceptor. *J Neurosci* 8(7):2334–2337.
40. Karpen JW, Loney DA, Baylor DA (1992) Cyclic GMP-activated channels of salamander retinal rods: Spatial distribution and variation of responsiveness. *J Physiol* 448:257–274.
41. Pugh EN, Jr, Lamb TD (1993) Amplification and kinetics of the activation steps in phototransduction. *Biochim Biophys Acta* 1141(2-3):111–149.
42. Koutalos Y, Nakatani K, Yau KW (1995) Cyclic GMP diffusion coefficient in rod photoreceptor outer segments. *Biophys J* 68(1):373–382.
43. Anderson DH, Fisher SK, Steinberg RH (1978) Mammalian cones: Disc shedding, phagocytosis, and renewal. *Invest Ophthalmol Vis Sci* 17(2):117–133.
44. Martinez-Marcos A, Jia C, Quan W, Halpern M (2005) Neurogenesis, migration, and apoptosis in the vomeronasal epithelium of adult mice. *J Neurobiol* 63(3):173–187.
45. Brann JH, Firestein S (2010) Regeneration of new neurons is preserved in aged vomeronasal epithelia. *J Neurosci* 30(46):15686–15694.
46. Brann JH, Firestein SJ (2014) A lifetime of neurogenesis in the olfactory system. *Front Neurosci* 8:182.
47. Yang H, He BR, Hao DJ (2015) Biological roles of olfactory ensheathing cells in facilitating neural regeneration: A systematic review. *Mol Neurobiol* 51(1):168–179.
48. Weinberg SH, Smith GD (2014) The influence of Ca^{2+} buffers on free $[Ca^{2+}]$ fluctuations and the effective volume of Ca^{2+} microdomains. *Biophys J* 106(12):2693–2709.
49. DerMardirossian C, Rocklin G, Seo JY, Bokoch GM (2006) Phosphorylation of RhoGDI by Src regulates Rho GTPase binding and cytosol-membrane cycling. *Mol Biol Cell* 17(11):4760–4768.
50. Ellis-Davies GC (2007) Caged compounds: Photorelease technology for control of cellular chemistry and physiology. *Nat Methods* 4(8):619–628.
51. Ellis-Davies GC (2008) Neurobiology with caged calcium. *Chem Rev* 108(5):1603–1613.
52. Wieboldt R, et al. (1994) Photolabile precursors of glutamate: Synthesis, photochemical properties, and activation of glutamate receptors on a microsecond time scale. *Proc Natl Acad Sci USA* 91(19):8752–8756.
53. Rial Verde EM, Zayat L, Etchenique R, Yuste R (2008) Photorelease of GABA with visible light using an inorganic caging group. *Front Neural Circuits* 2:2.
54. Volgraf M, et al. (2006) Allosteric control of an ionotropic glutamate receptor with an optical switch. *Nat Chem Biol* 2(1):47–52.
55. Banghart M, Borges K, Isacoff E, Trauner D, Kramer RH (2004) Light-activated ion channels for remote control of neuronal firing. *Nat Neurosci* 7(12):1381–1386.
56. Boyden ES, Zhang F, Bamberg E, Nagel G, Deisseroth K (2005) Millisecond-timescale, genetically targeted optical control of neural activity. *Nat Neurosci* 8(9):1263–1268.
57. Zhang F, et al. (2007) Multimodal fast optical interrogation of neural circuitry. *Nature* 446(7136):633–639.
58. Airan RD, Thompson KR, Fenno LE, Bernstein H, Deisseroth K (2009) Temporally precise in vivo control of intracellular signalling. *Nature* 458(7241):1025–1029.
59. Wu YI, et al. (2009) A genetically encoded photoactivatable Rac controls the motility of living cells. *Nature* 461(7260):104–108.
60. Häusser M (2014) Optogenetics: The age of light. *Nat Methods* 11(10):1012–1014.
61. Bianchi S, et al. (2013) Focusing and imaging with increased numerical apertures through multimode fibers with micro-fabricated optics. *Opt Lett* 38(23):4935–4938.
62. Marchesi A, Mazzolini M, Torre V (2012) Gating of cyclic nucleotide-gated channels is voltage dependent. *Nat Commun* 3:973.
63. De Palo G, et al. (2013) Common dynamical features of sensory adaptation in photoreceptors and olfactory sensory neurons. *Sci Rep* 3:1251.
64. Röhlich P, Szél A (2000) Photoreceptor cells in the Xenopus retina. *Microsc Res Tech* 50(5):327–337.
65. Caruso G, et al. (2010) Kinetics of rhodopsin deactivation and its role in regulating recovery and reproducibility of rod photoresponse. *PLOS Comput Biol* 6(12):e1001031.
66. Berek M (1927) Grundlagen der Tiefenwahrnehmung im Mikroskop. *Marburger Sitzungsberichte* 62:189–223.
67. Arimoto R, Saloma C, Tanaka T, Kawata S (1992) Imaging properties of axicon in a scanning optical system. *Appl Opt* 31(31):6653–6657.
68. Williams WB, Pendry JB (2005) Generating Bessel beams by use of localized modes. *J Opt Soc Am A Opt Image Sci Vis* 22(5):992–997.
69. Belyi V, Forbes A, Kazak N, Khilo N, Ropot P (2010) Bessel-like beams with z-dependent cone angles. *Opt Express* 18(3):1966–1973.